






Multilevel X-ray imaging approach to assess the sequential evolution of multi-organ damage in multiple sclerosis

Francesca Palermo ^{1,2}✉, Nicola Pieroni¹, Alessia Sanna^{1,2,3}, Benedetta Parodi⁴, Consuelo Venturi⁴, Ginevra Begani Provinciali^{1,5}, Lorenzo Massimi¹, Laura Maugeri ², Gian Paolo Marra², Elena Longo ⁶, Lorenzo D'Amico^{6,7}, Giulia Saccomano ^{6,7}, Jonathan Perrin⁸, Giuliana Tromba⁶, Inna Bukreeva¹, Michela Fratini^{1,9}, Giuseppe Gigli², Nicole Kerlero de Rosbo ^{1,4,10}✉ & Alessia Cedola^{1,10}✉

The 3D complexity of biological tissues and intricate structural-functional connections call for state-of-the-art X-ray imaging approaches to overcome limitations of classical imaging. Unlike other imaging techniques, X-ray phase-contrast tomography (XPCT) offers a highly sensitive 3D imaging approach to investigate different disease-relevant networks at levels ranging from single cell through to intact organ. We present here a concomitant study of the evolution of tissue damage and inflammation in different organs affected by the disease in the murine model for multiple sclerosis, a demyelinating autoimmune disorder of the central nervous system. XPCT identifies and monitors structural and cellular alterations throughout the central nervous system, but also in the gut, and eye, of mice induced to develop multiple sclerosis-like disease and sacrificed at pre-symptomatic and symptomatic time points. This study details the sequential evolution of multi-organ damages in the murine multiple sclerosis model showing the disease development and progression which is of relevance for the human case.

¹Institute of Nanotechnology—CNR, Rome, Italy. ²Institute of Nanotechnology—CNR, Lecce, Italy. ³Université Grenoble Alpes, Grenoble, France. ⁴Department of Neurosciences, Rehabilitation, Ophthalmology and Maternal-Fetal Medicine (DINOEMI), University of Genoa, Genoa, Italy. ⁵LOA, ENSTA Paris, CNRS, Ecole Polytechnique IP Paris, Palaiseau, France. ⁶Elettra - Sincrotrone Trieste S.C.p.A., Trieste, Italy. ⁷University of Trieste, Trieste, Italy. ⁸Synchrotron SOLEIL, Saint-Aubin, France. ⁹IRCCS Fondazione Santa Lucia, Laboratory of Neurophysics and Neuroimaging (NaN), Rome, Italy. ¹⁰These authors jointly supervised this work: Nicole Kerlero de Rosbo, Alessia Cedola. ✉email: francesca.palermo00@gmail.com; nkder.work@gmail.com; alessia.cedola@cnr.it

Multiple sclerosis (MS) is an inflammatory demyelinating disease, which results in a progressive damage to the structures of the central nervous system (CNS). It is the most common non-traumatic cause of neurological disability in young adults, but its etiology is still uncertain. MS is a complex and heterogeneous disease which presents variable clinical and pathological manifestations: inflammation process involving T cells, B cells, activated antigen-presenting cells and complement; demyelination, as a consequence of myelin attacked by the immune system and/or death of myelin-producing oligodendrocytes; axonal and neuronal damage and loss¹.

In the last decade or so, an increasing number of studies have reported the involvement of the gut-brain axis in neurodegenerative diseases, emphasizing the possibility that gut alterations lead to brain dysfunction, and suggesting that gut permeability might be one causal factor of several such diseases, including in particular Parkinson's disease². Although poorly described as yet, gut inflammation leading to intestinal barrier alteration and increased permeability has been reported in MS and its murine model, experimental autoimmune encephalomyelitis (EAE), and gastrointestinal manifestations are common in MS². In EAE, a histological study at 7 days post encephalitogenic challenge (prior to clinical disease onset) demonstrated intestinal permeability at ileum level in association with an infiltration of potentially pathogenic T cells in the lamina propria³. In the context of the temporality of gut versus brain inflammation in EAE, a recent study in adoptive EAE showed that the transferred encephalitogenic T cells infiltrated the colonic lamina propria, prior to the CNS, in the pre-clinical phase of EAE, and were later seen to reach the CNS of mice that had developed EAE symptoms. Blocking the entry of these cells to the large intestine in the early phase of EAE significantly attenuated the disease course and expression⁴. In line with these observations, it is noteworthy that demyelination, the hallmark of MS, has been observed consecutive to inflammatory bowel disease^{5,6}.

A well-recognized predictor of MS is optic neuritis, which is diagnosed in 75% of patients⁷. The eye is a unique window on the brain, with the retina and optic nerve originating as outgrowths of the developing brain. MS-related demyelination includes the optic nerve and the retinal nerve fibers, in addition to the brain and spinal cord. Optic neuritis has also been demonstrated in EAE, associated with inflammatory cell infiltrates and optic nerve atrophy^{8–10}. Since axons in the optic nerves are closely connected to the nerve fiber layer and ganglion cells, degenerative processes involving the optic nerve might produce also retinal alterations, consisting in thinning of the nerve fiber layer and ganglion cell loss^{11,12}.

X-ray phase contrast tomography (XPCT) provides a highly sensitive 3D tool for the investigation of biological soft tissues, without sectioning, staining or exposing samples to intense tissue processing¹³. XPCT enables a simultaneous biomedical imaging of different structures, such as the vascular and neural networks^{14–16}, and, most importantly, it generates a multiscale image - ranging from the cell through to the organ as a whole - that permits the study of the interaction of single element(s) with the surrounding micro-environment^{17–19}.

Here, we present a multi-organ XPCT investigation in EAE covering the CNS, gut, and eyes of mice, to monitor early imaging indicators potentially acting as biomarkers of pathological processes in these organs. This approach rests on a multiscale analysis of each organ detecting early appearance of alterations at different phases of disease in different tissues. Therefore, the longitudinal data obtained can permit an original evaluation of the temporal progression of the disease in the different anatomical sites. The possibility to assess concomitantly the temporal alterations in the different target organs, and eventually obtain

quantitative data with sufficient samples tested, could serve to put together imaging signatures that define progression states.

Results

To monitor disease development and uncover possible pre-symptomatic disease-related structural and cellular alterations, we used XPCT to obtain 3D images of CNS, gut and eye in EAE-induced mice at different time points following immunization with myelin oligodendrocyte glycoprotein peptide 35–55, spanning very early asymptomatic stage, i.e., 3 days post induction (dpi), to asymptomatic inflammatory phase (5/7 dpi) through to disease onset (11–13 dpi).

XPCT allows direct detection of blood-CNS barrier disruption in EAE. We first investigated the disruption of the blood-brain and blood-spinal cord barriers (BBB/BSCB), which is a crucial hallmark in the pathogenesis of MS and EAE. The impairment of the barrier manifests as an alteration in its permeability which favors subsequent infiltration of immune cells and immune mediators into the CNS. We analyzed the brain and spinal cord in naïve mice as control and in EAE-induced mice, focusing on the lumbar spinal cord region, which is first affected since the temporal pattern of the EAE lesions exhibits a caudo-rostral progression²⁰. Ex-vivo XPCT images were obtained of the organs isolated from mice sacrificed at the selected time points. Figure 1 demonstrates the progressive degeneration of the vascular system through the appearance of “clouds”, visible as halos around the vessels. These clouds are compatible with extravasated material, which includes inflammatory cells and blood components. The presence and the extension of the clouds can be assumed as a criterion to assess the increasing BBB/BSCB permeability and, consequently, the ongoing inflammatory process. Figure 1(a–d) shows representative tomographic images of a sample of lumbar spinal cord in sagittal view for each time point (naïve, 3 dpi, 7 dpi, and disease onset). The tomographic images have a voxel size of $3.05 \times 3.05 \times 3.05 \mu\text{m}^3$. In order to highlight the vasculature, we applied the maximum intensity projection procedure (Methods). The different gray-levels correspond to different densities inside the sample: structures with higher density appear brighter than the surrounding tissue. We have chosen to use non-perfused samples to preserve the blood components inside them. Indeed, because of the presence of proteins which bind and carry metals, such as hemoglobin, transferrin and albumin, blood acts as an endogenous contrast agent, highlighting the blood vessels and the extravasated material²¹. The micrometric spatial resolution allows the visualization of the distribution of vessels with diameters ranging from 10 to 35 microns.

In all the samples, we can observe vessels arising from the longitudinal anterior spinal artery, visible as a white stripe running along the right vertical edge of the spinal cord. In the lumbar spinal cord of EAE-induced mice at 7 dpi and onset (Fig. 1c, d), these vessels appear surrounded by numerous clouds of an intermediate level of gray, which are not observed in the spinal cord of naïve mice or of EAE-induced mice at 3 dpi (Fig. 1a, b).

Quantification of vascular damage at different time points is shown in the bar chart reported in Fig. 1e. We analyzed $n = 3$ samples for each group (naïve, 3 dpi, 7 dpi, onset), defining as damaged vessels those with clouds in their surroundings, such as those highlighted in the insets of Fig. 1f, g and indicated by the arrows. The vascular damage is thus expressed as the number of the detected vessels surrounded by clouds over the total number of visible vessels in the whole lumbar spinal cord region. At 3 dpi, the first time point tested, damaged vessels are not visible. At 7 dpi, corresponding to an early inflammatory phase of the disease,

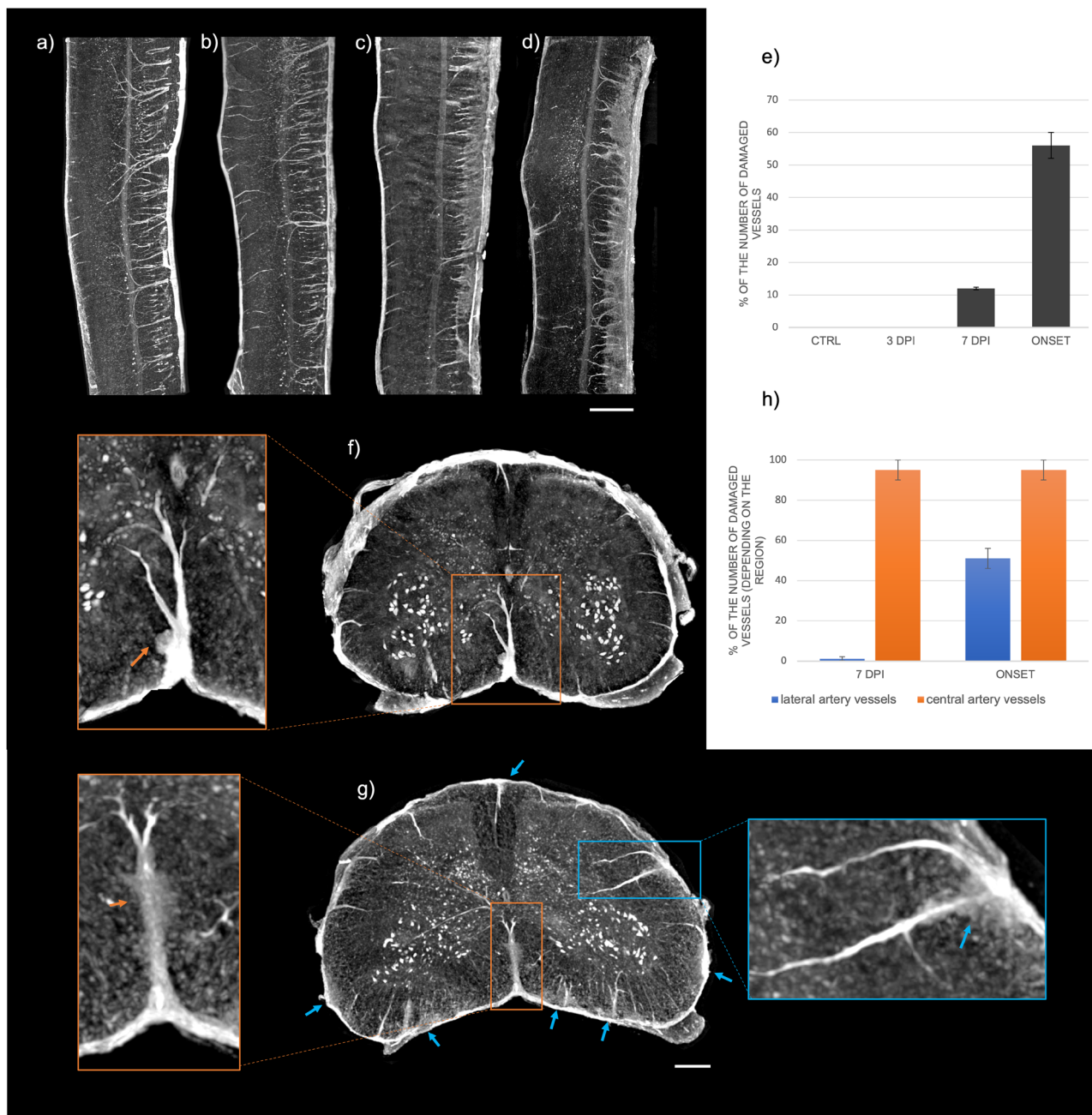


Fig. 1 Blood-spinal cord barrier leakage and lesion in lumbar spinal cord. The images show X-ray phase contrast tomography (XPCT) imaging and quantification of blood-spinal cord barrier leakage and lesion in lumbar spinal cord of experimental autoimmune encephalomyelitis (EAE)-induced mice. **a-d** XPCT images showing the sagittal views of the lumbar spinal cord in a naïve mouse (**a**) and in EAE-induced mice at 3 days post induction (dpi) (**b**), 7 dpi (**c**), and disease onset (**d**). In (**c**) and (**d**) the vessels arising from the anterior spinal artery appear surrounded by numerous clouds of extravasated material reflecting the intense blood-spinal cord barrier dysfunction in the EAE-induced mice. Scale bar = 500 μ m. **e** Quantification of the number of damaged vessels with respect to the total number of vessels in lumbar spinal cord samples of EAE-induced mice ($n = 3$ per group). The data are presented as mean \pm SEM. **f, g** XPCT images showing the axial view of lumbar spinal cord of EAE-induced mice at 7 dpi (**f**) and onset (**g**). The insets and the arrows highlight the presence and the localization of clouds. At 7 dpi (**f**), vascular degeneration appears to involve vessels arising from the anterior spinal artery (inset). In contrast, at onset (**g**) the lesion becomes more extensive, involving also vessels arising from minor arteries (arrows and blue inset). Scale bar = 200 μ m. **h** Quantification of the number of damaged vessels over the total number of vessels, separately for vessels originating from the central artery (orange) and for vessels originating from secondary arteries and venules (blue), in lumbar spinal cord samples from EAE-induced mice at 7dpi and onset ($n = 3$ per group). The data are presented as mean \pm SEM. Clinical EAE score at the onset = 3. Images **a-d, f, g** were obtained as maximum intensity projections of XPCT volumes (**a-d** over 150 μ m; **f, g** over 100 μ m). XPCT images were acquired in Experiment 1, reported in Methods.

about 10% of the vessels were damaged; this value increased to 55% at disease onset.

By measuring vascular damage separately for vessels originating from the central artery and vessels originating from secondary

arteries and venules, over time, we aimed at defining how vascular alteration spreads in lumbar spinal cord. As mentioned above, at 7 dpi, vascular degeneration largely involves vessels arising from the anterior spinal artery, as seen in Fig. 1c, f, which present the

sagittal and axial views of a representative 7 dpi lumbar spinal cord, respectively. The zoom in Fig. 1f highlights the presence of a small cloud (indicated by the arrow) close to a vessel originating from the central artery. However, at that pre-symptomatic time, lesions are not visible around vessels arising from other arteries or venules. In contrast, at the onset of the disease, both vessels from the central artery and vessels from the minor arteries appear significantly damaged, as visible in Fig. 1d, g, showing the sagittal and axial views of a representative lumbar spinal cord at onset, respectively. The zooms in Fig. 1g highlight the presence of clouds around numerous vessels (arrows). Note that the clouds are mainly located at the base of the vessels.

Quantification of the number of damaged vessels measured separately for vessels originating from the central artery and for vessels originating from secondary arteries and venules is reported in Fig. 1h. The vessels from the central artery appear to be almost all involved in the inflammatory process from 7 dpi. On the other hand, for vessels originating from secondary arteries, we observe a sharp increase in damaged vessels from 15% at 7 dpi to 50% at onset, reflecting how the lesion becomes more extensive at this stage.

High resolution tomographic images (voxel size of $0.65 \times 0.65 \times 0.65 \mu\text{m}^3$) allowed the visualization of the clouds as including a large accumulation of cells localized around the vessels (Fig. 2a), which would be commensurate with infiltrating inflammatory T cells and macrophages typical of an EAE lesion. The rendering reported in Fig. 2b provides a 3D morphological description of the surroundings of this lesion, where the structures of interest are segmented in different colors. We can observe how the clouds of extravasated material (gray), which include the infiltrating cells, completely surround the base of the vessels (yellow). In the neural network, we could distinguish cells with morphology commensurate with nonspecific neuron-like

cells and multipolar neuron-like cells, rendered in green and blue, respectively.

The tomographic images and the 3D rendering of the spinal cord displayed in Fig. 2c–f demonstrate the level of detail achievable with micro-XPCT, which allows a thorough imaging of the micro-environment at neuronal and vascular levels. Simultaneous 3D visualization of these details, which provide the real surroundings of the alteration point, is a specific prerogative of the XPCT technique. Figure 2c shows cells located in the anterior horn of the spinal cord compatible with neurons provided with processes, dendrites, or axons. A 3D-rendering of the neuro-vascular micro-environment is shown in Fig. 2d, where cells compatible with neurons (blue) are surrounded by capillaries (yellow). The 3D representation emphasizes the distribution in space of the neural and vascular components. As observed in Fig. 2e, f (white arrows), dashed structures were detected, which could be compatible with neural axons wrapped by sheaths of myelin, an extension of oligodendrocyte plasma membrane, periodically interrupted by the so-called nodes of Ranvier. Of note, in Fig. 2e, the myelinated axon (white arrow) seems to become less bright and to lose its periodicity as it approaches the EAE vascular lesion (yellow arrow).

Along with the spinal cords, we measured brains dissected from the same mice, to assess the anatomical progression of the vascular damage throughout the CNS of EAE-induced mice. Figure 3a shows the posterior brain region of a mouse at onset, where cerebellum, brainstem, and cervical spinal cord regions are visible. Tomographic images in Fig. 3b, c, which represent a portion of brainstem and cervical spinal cord in coronal view, respectively, demonstrate the presence of clouds and cell accumulation (highlighted by arrows) in these sites at the clinical onset. Although present to a lesser extent with respect to the lumbar spinal cord region, BBB/BSCB damage appears to have reached upper spinal cord and brainstem at clinical onset,

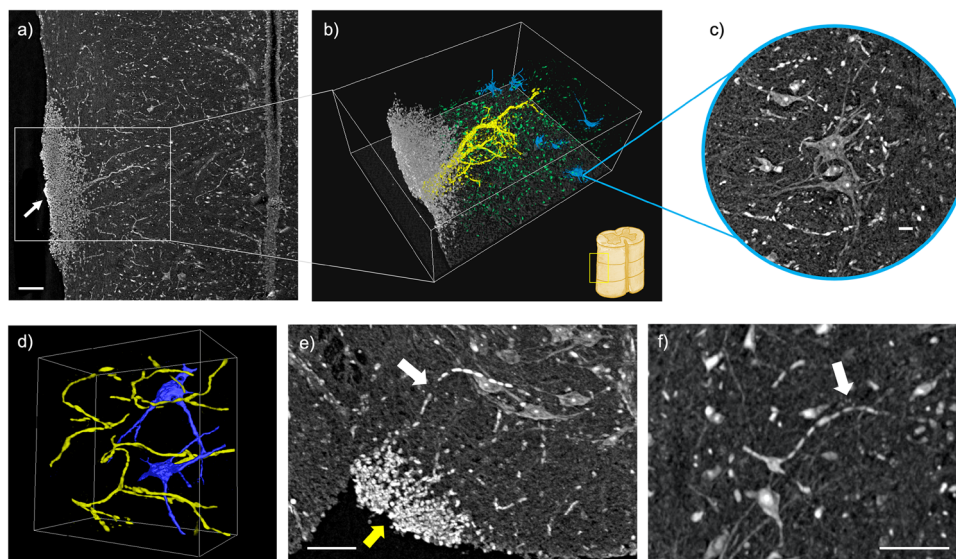


Fig. 2 Micro-environment of vascular lesions in lumbar spinal cord. High-resolution X-ray phase contrast tomography (XPCT) describes the micro-environment of vascular lesions in lumbar spinal cord of an experimental autoimmune encephalomyelitis (EAE)-induced mouse at disease onset. **a** XPCT image showing a portion of the lumbar spinal cord in coronal view. The arrow highlights the presence of a lesion with a large accumulation of cells around vessels. Scale bar = $50 \mu\text{m}$. **b** 3D-rendering of the micro-environment around the vascular lesion. The features are segmented with different colors: in white the small cells surrounding the vessel (yellow), in green and blue morphologically neuron-like cells. Inset: schematic representation of the localization of the vascular lesion of (**a**) and (**b**) in the spinal cord. The image was obtained by reprocessing the data used to produce a figure from our recent work²¹. **c** XPCT image of star-shaped cells located in the anterior horn of EAE-induced mouse, compatible with neurons provided with processes, dendrites, or axons. Scale bar = $25 \mu\text{m}$. **d** 3D-rendering of star-shaped cells (blue) surrounded by capillaries (yellow). **e**, **f** XPCT images with well-visible dashed structures (white arrows) compatible with axons wrapped by myelin sheath (scale bar = $50 \mu\text{m}$). In (**e**), near the lesion (yellow arrow) the dashed structure seems to lose its periodicity and to become less bright (white arrow). Clinical EAE score at the onset = 1.5. Images **a–c**, **e**, **f** were obtained as maximum intensity projections of XPCT volumes (**a** over $15 \mu\text{m}$; **c** over $10 \mu\text{m}$; **d**, **e** over $10 \mu\text{m}$). XPCT images were acquired in Experiment 2, reported in Methods.

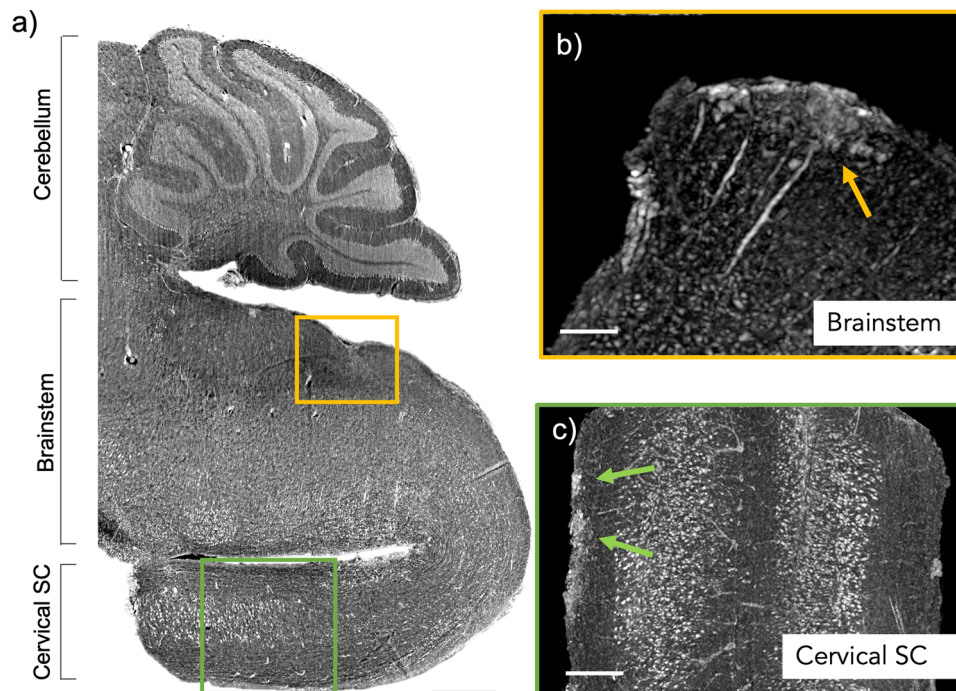


Fig. 3 Vascular damage in brain and cervical spinal cord at clinical onset. X-ray phase contrast tomography (XPCT) shows vascular damage in experimental autoimmune encephalomyelitis (EAE) brain and cervical spinal cord at clinical onset. **a** XPCT image showing a representative sagittal view of cerebellum, brain stem, and cervical spinal cord of an EAE-induced mouse at disease onset. The yellow and green squares indicate respectively where the lesions showed in **(b)** and **(c)** are located. Scale bar = 500 μm . **b** XPCT image of a detail of the brainstem at EAE onset, with the presence of clouds (indicated by the yellow arrow) at the base of the vessels (scale bar = 50 μm). **c** XPCT image showing coronal view of the cervical spinal cord of an EAE-induced mouse at onset. Green arrows highlight the vascular lesions (scale bar = 150 μm). Clinical EAE score at the onset = 1.5. Images were obtained as maximum intensity projections of XPCT volumes (**a** over 150 μm ; **b** over 80 μm ; **c** over 100 μm). XPCT images were acquired in Experiment 3, reported in Methods.

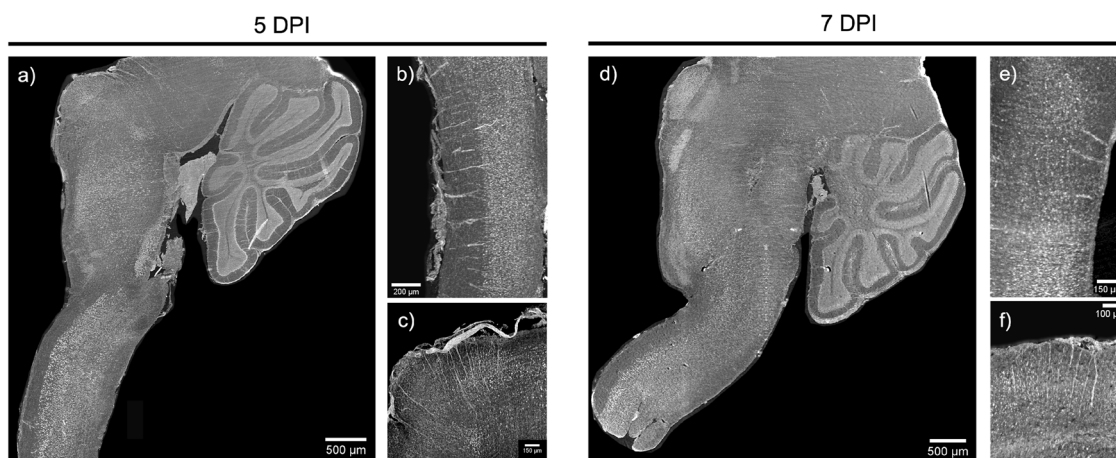


Fig. 4 Brain and cervical spinal cord at presymptomatic stages. X-ray phase contrast tomography (XPCT) images of brain and cervical spinal cord of 5 days post induction (dpi) and 7dpi EAE-induced mice. **a** Sagittal view of cerebellum, brain stem, and cervical spinal cord of a 5dpi EAE-induced mouse (scale bar = 500 μm). **b** Coronal view of a portion of the cervical SC of a 5 EAE-induced mouse (scale bar = 200 μm). **c** XPCT image of a detail of the brainstem at 5dpi (scale bar = 150 μm). **d** Sagittal view of cerebellum, brain stem, and cervical SC of a 7dpi EAE-induced mouse (scale bar = 500 μm). **e** Coronal view of a portion of the cervical SC of a 7dpi EAE-induced mouse (scale bar = 150 μm). **f** XPCT image of a detail of the brainstem at 7dpi (scale bar = 100 μm). Images were obtained as maximum intensity projections of XPCT volumes (**a** over 130 μm ; **b** over 100 μm ; **c** over 80 μm ; **d** over 150 μm ; **e** over 80 μm ; **f** over 80 μm).

whereas vascular alterations in these regions are not observed at pre-symptomatic time points (Fig. 4). These results corroborate the temporal course of BBB dysfunction in EAE, with increased permeability proceeding along from the lumbar spinal cord to the brain^{20,22}, and confirm XPCT as a high-resolution technique able to detect even subtle alterations of the blood barriers.

XPCT allows the detection of variations in cell density in ileal villi in EAE. To investigate whether there is a temporal correlation between CNS and gut alterations, we sought to identify imaging markers for the inflammation processes that involve the intestine of EAE-induced mice. To reveal changes between normal and pathological conditions, the gut morphology needs to be

examined, but the complex geometry and structural convolutions of the gut prevent the identification of sample features. Anatomically, the gut looks like a long tube of varying diameter with flexible walls, folded several times on itself, as illustrated by 3D rendering in Fig. 5a. To extract morphological details, we reduced the geometrical complexity by virtual flattening. The gut cylindrical surface was mapped into a plane by means of flattening algorithms described in Methods. These procedures allow the visualization of structures otherwise very hard to recognize in the 3D volume. Figure 5b–d illustrate some morphological features of the small intestine wall, displayed on 2D plane upon virtual flattening. We can distinguish the thin longitudinal layer of smooth muscle fibers belonging to the tunica muscularis (Fig. 5b), cells compatible in shape, dimension, and location with neurons of the myenteric plexus^{23,24} (Fig. 5c), and blood vessels (Fig. 5d) running along the tela submucosa.

XPCT does make possible the multiscale 3D imaging of the tissues, ranging from the intestine as a whole (Fig. 5a) down to the single cell (Fig. 5b), thereby overcoming the limitations of histology/immuno-histochemistry. Indeed, although histology/immuno-histochemistry provides very informative and resolved 2D images of biological tissues, it requires destructive sample preparation to thin the sample down to hundreds of microns and subsequently restricts spatial coverage within a finite depth. However, in contrast to immuno-histochemistry which identifies a cell through its staining of markers recognized by specific antibodies, XPCT cannot identify a cell other than through its morphological aspect, together with its location. Nevertheless, XPCT can reproduce in 3D the morphological features visible in the histological sections with a similar spatial resolution. The comparison between a hematoxylin-eosin stained histological section and an XPCT image of villi from a naïve mouse ileum (Fig. 5e, f, respectively) demonstrates that XPCT can indeed achieve histology-like resolution. A 3D rendering from XPCT data of an ileal villus is shown in Fig. 5g, where blood vessels are segmented in red, lymphatic canals in blue and cell nuclei in yellow.

In some models of EAE³, intestinal barrier permeability, together with morphological alterations, was observed already at 7 dpi and was associated with an increase in potentially pathogenic T cells infiltrating the gut lamina propria^{3,25}. In order to identify an imaging marker of EAE detectable with XPCT, we measured the density of cells located in this area, limited to the region of the villi, at different time points of the disease, i.e., 3 dpi, 7 dpi and EAE onset. We define cell density as the number of cells detected per unit volume.

Because XPCT does not allow the identification of specific cells, if not for morphological or location considerations, to exclude epithelial cells and select only the cells located in the lamina propria we quantified the variation over time in cell density in the area delineated by the red line in Fig. 5h, which shows a 3D-rendering of a villus segmented to highlight the spatial distribution of cell nuclei (in yellow) inside the volume.

We analyzed $n = 2$ ilea for each time point in EAE-induced mice (3 dpi, 7 dpi, EAE onset) or naïve mice. Measurements of cell density were performed on approximately 20 villi per ileum. Quantification of cell density is shown in Fig. 5i, where we observe an increment at clinical onset.

However, because of the large variability we have detected in the villi population of a single mouse and among different mice, we do not claim to have obtained conclusive results. To achieve statistical significance, it will be necessary to measure more samples so as to limit the variability effect. Nevertheless, our results indicate that XPCT and the described procedures are fully suitable to perform both qualitative and quantitative investigations at high resolution.

XPCT reveals inflammatory infiltrates and atrophy of the optic nerve at EAE onset. Visual deficits are relevant symptoms in MS and EAE. Neuropathological alterations in the retina and the optic nerve occur, including thinning of retinal fiber layers, losses in retinal ganglion cells, demyelination and activation of microglia and astroglia, and inflammatory cell infiltration.

The accessibility of the retina through advanced non-invasive ocular imaging techniques makes it a potential convenient site for the research and diagnosis of diseases affecting the CNS. For this reason, it is essential to identify imaging markers in the eye and to temporally correlate them to the progression of the disease in the other relevant anatomical sites.

Figure 6a, b show XPCT images of the optic nerve in longitudinal view, near the point where it enters the retina, partially visible at the top of the images, in a naïve mouse (Fig. 6a) and an EAE-induced mouse (Fig. 6b). The dashed lines define the location of the axial sections reported in Fig. 6c and d. In both longitudinal and axial view of the EAE optic nerve (Fig. 6b, d), XPCT reveals clear alterations represented by large accumulations of inflammatory cell infiltrates (highlighted by the arrows) compatible with the occurrence of optic neuritis. Moreover, the longitudinal view in Fig. 6b clearly shows atrophy of the optic nerve.

The XPCT technique provides a feasible means to detect the structure of blood vessels, and we are interested in studying the vasculature of the eye over an area as large as possible. Blood vessels in the eye are confined mainly within very thin spherical layers and optimal visualization of this vascular network is possible only upon virtual flattening. Moreover, deformations can occur upon embedding the samples in the media, as seen in Fig. 6e, which shows a section of naïve mouse eye imaged by XPCT. The outer layers of the eye collapsed onto the lens (the circular shape structure in the center) and curled up since the vitreous contained within the eye dried out. Therefore, to investigate the ocular vascularization, virtual flattening procedures are mandatory. Once the spherical surface of the eye has been virtually flattened, the different layers can be studied by simply performing virtual slicing parallel to the plane of the layers. Representative results of virtual flattening, performed by means of algorithms described in Methods, are shown in Fig. 6f, g, which show a lateral section of the retina and the en face surface of the choroidal layer, respectively. The choroid (Fig. 6g) is a highly vascularized structure that separates the sclera from the retina. XPCT images were quantified and we measured the diameter of the visible vessels, which ranged from 5 to 20 microns.

Unfortunately, the eye samples in this study were only available to assess EAE onset vs naïve status, and the comparison with intermediate time points was not possible. Nevertheless, as CNS pathology in EAE progresses in a caudo-rostral fashion with time and we did not detect any damage in the brain at pre-symptomatic time points, we would expect that this also applies to disease progression in the eye at the same time points. While the message of this report is intended to be that of demonstrating the power of XPCT in assessing fine alterations concomitantly in different organs, we have an ongoing larger study including intermediate time points for the eye to provide a definitive biological message.

Sequential evolution of pathological alterations of EAE over time in the investigated anatomical sites. We have monitored pathological features of EAE at pre-symptomatic and/or early stages of the disease in each of the considered anatomical regions, i.e., brain, spinal cord, gut, and optic nerve. The observed alterations are of different nature and appear at different time

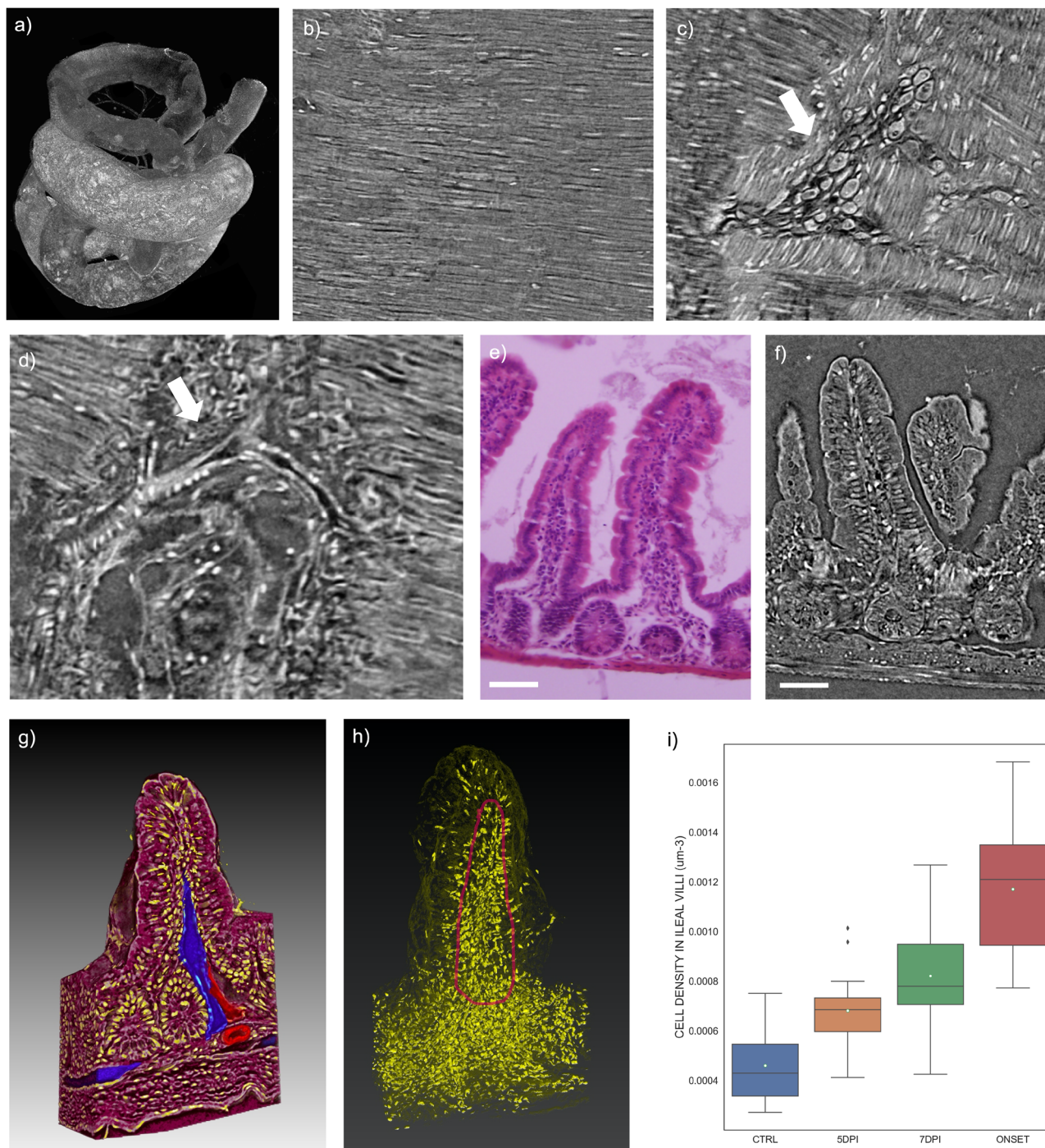


Fig. 5 Multiscale imaging of mouse gut and cell density in lamina propria of ileal villi. X-ray phase contrast tomography (XPCT) enables multiscale imaging of mouse gut with histology-like resolution and quantification of cell density in lamina propria of ileal villi. **a** 3D-rendering of a whole mouse gut from a naïve mouse imaged with XPCT. **b–d** XPCT images of the layers of gut wall obtained after virtual flattening of the ileum of an experimental autoimmune encephalomyelitis (EAE)-affected mouse. **b** Tunica muscularis; **c** cells compatible in size, morphology, and location with neurons of the myenteric plexus^{23,24} (arrow); **d** vessel (arrow) running along the tela submucosa. **e** Hematoxylin-eosin stained histological section and **f** XPCT image of ileal villi of an EAE-affected mouse. The XPCT image was obtained as maximum intensity projections over 5 µm. Scale bar = 50 µm. **g** 3D-rendering from XPCT data of a villus from the ileum of an EAE-affected mouse; blood vessels are segmented in red, lymphatic canals in blue, and cells in yellow. **h** 3D-rendering of the cells inside the volume of a villus from the ileum of an EAE-affected mouse; the area outlined by the red line roughly corresponds to the region of the lamina propria. **i** Box plot of cell density calculated as the ratio of the number of cells counted in the lamina propria to the volume occupied by this structure in the villus (20 villi per $n = 2$ mice per time point). Mean values are indicated by white spots and outliers are presented as black spots. Clinical EAE score at the onset = 1.5. XPCT data were acquired in Experiment 2, reported in Methods.

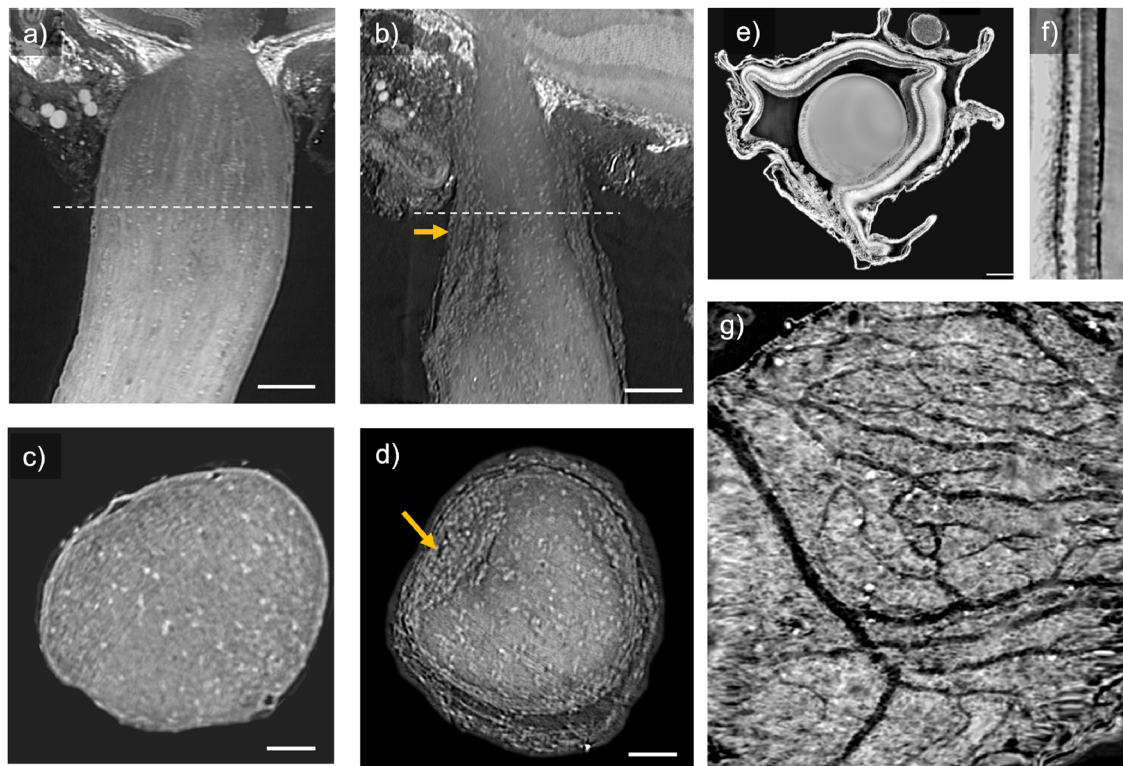


Fig. 6 Pathological alterations in optic nerve. X-ray phase contrast tomography (XPCT) shows pathological alterations in experimental autoimmune encephalomyelitis (EAE) optic nerve and allows the visualization of ocular vascularization. **a–d** XPCT images showing the longitudinal (**a, b**) and axial (**c, d**) views of the optic nerve in a naive mouse (**a, c**), and an EAE-induced mouse at disease onset (**b, d**), where large accumulations of inflammatory cell infiltrates (arrows) compatible with the occurrence of optical neuritis are visible. The dashed lines in (**a, b**) illustrate the location of the axial sections (**c, d**). Scale bar (**a, b**) = 100 μm . Scale bar (**c, d**) = 50 μm . **e** XPCT image showing a section of ocular bulb from a naive mouse. Structural deformations due to sample preparation in paraffin are visible. Scale bar = 200 μm . **f, g** Representative results of virtual flattening of a naive mouse eye: lateral section of retina (**f**) and the en face surface of the highly vascularized choroidal layer (**g**). Samples presented in **a–d** and **g** were embedded in epon, whereas samples presented in **e** and **f** were embedded in paraffin. Clinical EAE score at the onset = 2.5. XPCT images were acquired in Experiment 4, reported in Methods.

points, depending on the location. In the CNS, we observed the impairment of the vascular system through the appearance of clouds revealing the presence of extravasated material due to the pathological increase in BBB permeability; in the gut, XPCT permitted the monitoring of cellular infiltrates increasing over time from disease induction to onset; at the level of the optic nerve, a large accumulation of infiltrating cells and atrophy were detected at onset. Figure 7a summarizes with a visual schematization the results obtained through XPCT. In the lumbar spinal cord and gut, pathological alterations (PA) were identified as early as the pre-symptomatic stage (spinal cord, 7 dpi; gut, 5 and 7 dpi), whereas changes appeared at a later time in the brain (onset; no changes were detected at earlier time points, see Fig. 4), as expected.

Since we handle heterogeneous data that describe the PA through the quantification of the presence of distinctive markers as described above, to compare the extent of PA involving the different organs we introduced the parameter, referred to as PAR, being the ratio of PA at a certain time point over PA at the onset (see Methods). The PA has been calculated as the percentage of damaged vessels in the CNS, and in the gut as the variation in cell density with respect to the control.

In Fig. 7b, we show the spatial distribution of PAR revealed by XPCT at 7 dpi in the CNS and gut, to emphasize the appearance of imaging markers of EAE as early as the pre-symptomatic stage. At this time point, the PA reflected by the imaging markers of BBB permeability is not yet visible in the brain. At the same stage, however, we observe that both the spinal cord and the gut exhibit

some grade of PA expressed through PAR. While it is not surprising to observe changes in the spinal cord already from a pre-symptomatic stage, it is relevant to note that alterations in the gut at that time point are already observed, corroborating and reinforcing the findings of a previous 2D study³. In this framework, Fig. 7c depicts the temporal distribution of PA, expressed as PAR, appearing in the gut; thus, PA, already appreciable in the pre-symptomatic stages as early as 5 dpi, increase further at clinical onset.

Discussion

Here, we present a 3D multi-organ longitudinal study of tissue alterations that occur in different potential target organs throughout EAE, the experimental model for multiple sclerosis, and which we were able to describe and follow by XPCT. This technique allowed us to analyze the organ as a whole, which is not possible with 2D techniques such as immunohistochemistry nor with conventional 3D imaging. Thus, the possibility to assess the disruption of the BSCB as a whole organ enabled the observation of leakage from the vessels originating from the central artery already at 7 dpi, whereas the vessels originating from the lateral arteries were considerably less involved. At disease onset, the leakage in the spinal cord appeared massive, commensurate with the appearance of clinical signs, which at early stages are associated with vasogenic oedema^{20,26}. Permeability of the BBB was originally assessed with 2D techniques through detection of extravasated plasma proteins²⁰ or tracers, such as FITC-labeled

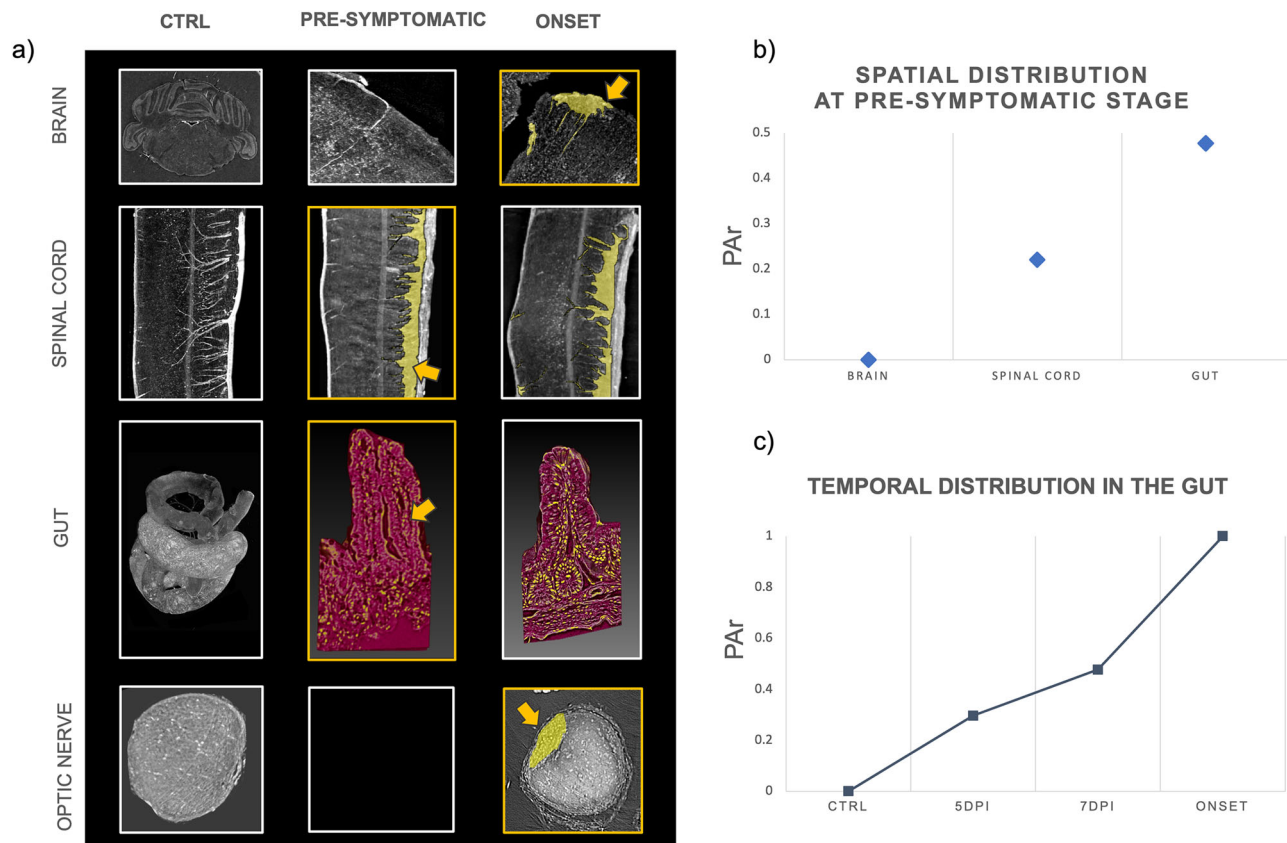


Fig. 7 Multi-organ investigation and temporal assessment of imaging markers at early stages. The figure shows the results of the multi-organ investigation and temporal assessment of experimental autoimmune encephalomyelitis (EAE) imaging markers at early stages. **a** Representative X-ray phase contrast tomography (XPCT) images and/or rendering of the multi-organ investigation of EAE at pre-symptomatic stage and at the onset. The arrows highlight the presence of alterations. In the brain, the degenerative process involves vascularization as well as in the spinal cord. In the gut and optic nerve, we detected imaging alteration through an increase in cellular infiltrates. The image for the optic nerve at the pre-symptomatic stage was not included because samples at this stage were not available. **b** Graphical representation of spatial distribution of PAR at 7 days post induction (dpi) ($n = 2$ samples for brain, $n = 3$ for spinal cord, $n = 2$ for gut). Optic nerve results were not included because samples were not available for this time point. **c** Distribution over time of the appearance of imaging markers for the gut in EAE-induced mice (20 villi per $n = 2$ mice per time point). Clinical EAE score at the onset = 1.5, 3, 1.5, 2.5.

high-molecular weight dextran that can be seen as fluorescent clouding of the vessels^{27,28}, or through examination of vascular changes and leakage in the CNS by immunostaining tissue slices for the endothelial marker CD31 and fibrinogen²⁹ or tight junction proteins³⁰. The latter technique enabled the demonstration of BBB damage as early as 4 dpi. However, 2D techniques do not permit the evaluation of the whole organ, and immunohistochemistry in particular requires considerable processing which can be fraught with artefacts. Accordingly, in the last twenty years or so, studies have used 3D techniques such as magnetic resonance imaging (MRI) to assess the BBB/BSCB in EAE. Through MRI, Schellenberg et al. observed a greater contrast enhancement in peripheral regions of the spinal cord in mice with symptomatic EAE³¹, as we observed by XPCT in mice immunized for EAE four days before clinical onset. The authors state that MR images in mice obtained at two days prior to clinical onset did not show any contrast enhancement, which, together with our XPCT data, suggests that MRI might not be as sensitive a technique as XPCT to follow the appearance of BSCB permeability. In another, relapsing-remitting, adoptive transfer model of EAE in mice, increases in barrier permeability was monitored in the CNS by molecular MRI using a gadolinium-based MRI probe that binds to fibrin; fibrin deposition was clearly observed at disease onset, increasing as disease progressed, and preceded cellular extravasation³². Unfortunately, the study did

not include pre-symptomatic stages. In Lewis rats with acute monophasic EAE, gadolinium enhancement preceding cellular extravasation was also observed from clinical onset; no difference was seen in pre-symptomatic rats compared to control rats²².

Interestingly, the molecular MRI technique also permitted the detection of fibrin deposits in the optic chiasm and optic nerve at disease onset³². Very few studies report longitudinal MRI analyses of the visual tract in EAE, and it is also generally not used to study the optic nerve or retinal lesions in MS. Nevertheless, MRI analysis in guinea pig EAE suggests that damage to the blood optic nerve barrier occurs early after disease induction, prior to clinical onset³³. In the present study, XPCT of the optic nerve of EAE-affected mice enabled the clear visualization of a massive inflammatory lesion in the optic nerve, accompanied by nerve atrophy; such observations have only been made previously in EAE with 2D histology techniques^{34,35}, with some evidence of inflammation and demyelination already at 7 dpi³⁶. Analysis of optic nerve damage is most often performed in MS using optical coherence tomography. In EAE, it has permitted the monitoring of retinal changes to predict neuronal loss at the chronic phase³⁷. However, optical coherence tomography does not enable the visualization of infiltrating cells such as we see with XPCT. Although the number of eyes measured is not enough to enable robust statistical analysis, the scope of this study was to obtain a

proof-of-concept that XPCT would yield high-quality images of different organs that would permit quantitative analysis for a reliable multi-organ assessment of EAE progression. A larger experiment including a larger number of samples to provide significant biological information is ongoing to enable us to determine the temporal pathological onset and the organ in which it initiates. Complementary techniques, such as X-ray microdiffraction³⁸ are also scheduled to provide additional structural information.

Although it is now recognized that gastrointestinal manifestations are frequent in MS, and gut inflammation has been described in EAE, little is known as yet about the structural and/or cellular alterations in the gut of EAE animals. Nevertheless, a decrease in intestinal barrier integrity, together with morphological alterations, was observed in mice induced for EAE prior to clinical disease onset³ and our recent publication³⁹, which combined XPCT and immunofluorescence analysis, reported morphological alterations accompanied by infiltration of inflammatory cells in mice with ongoing disease³⁹. In the present study, 3D XPCT permitted the clear visualization of the massive cellular infiltration in the villi. Although we had observed cellular infiltration of the villi by immunofluorescence in ongoing disease³⁹, XPCT enabled us to obtain a more pertinent quantitative evaluation based on the 3D volume of the villi, and therefore a longitudinal monitoring of cellular infiltration, which showed a peak at clinical disease onset and had decreased four days after. Such data are possibly commensurate with the observation that, in EAE induced by adoptive transfer of encephalitogenic T cells, these cells infiltrate the gut lamina propria at an early stage of EAE when they are not detected in the CNS, but can be traced to the CNS at a later stage, when they have decreased in the gut⁴.

In conclusion, in this work we describe the sequential evolution of damage in different organs within a murine model of MS showing how and where the disease develops and progresses, which is of obvious relevance for the human case. These results also demonstrate the power of the XPCT technique, which, being able to image on equal footing all tissues, including those classically considered invisible, allows for a multi-organ analysis without the use of contrast agents. Moreover, the possibility to image the whole organ down to the single cells in a multilevel approach is of great value with respect to the other techniques routinely used for these studies.

Methods

EAE induction and sample preparation. Female C57BL/6J mice, 6 to 8 weeks old, weighing 18.5 g purchased from Harlan Italy, were immunized as described before⁴⁰ by subcutaneous injection (200 µl total) at two sites in the flank with an emulsion of 200 mg myelin oligodendrocyte glycoprotein peptide 35–55 (Espikem) in incomplete Freund adjuvant (Difco) containing 600 mg Mycobacterium tuberculosis (strain H37Ra; Difco). The mice were injected (100 µl total) in the tail vein with 400 ng pertussis toxin (Sigma-Aldrich) immediately and 48 h after immunization. The mice were scored daily for clinical manifestations of EAE on a scale of 0–5⁴⁰, and sacrificed by CO₂ inhalation at different time points, before and at the onset of clinical manifestations (around day 11 after immunization), with a clinical score of 2.3 ± 0.9 . Samples obtained consisted of brain (EAE-induced mice at 3 dpi, 7 dpi, and disease onset; naïve mice), lumbar/sacrocoxygeal (L1–S4) spinal cord (EAE-induced mice at 3 dpi, 7 dpi, and disease onset; naïve mice), gut (EAE-induced mice at 5 dpi, 7 dpi, and disease onset; naïve mice) and eyes (EAE-induced mice at disease onset; naïve mice). Mice were not perfused to preserve the blood inside the vessels²¹. Further preparation steps were required depending on the experimental conditions under which they were to be measured.

All animals were housed in pathogen-free conditions and treated according to the Italian and European guidelines (Decreto Legislativo 4 marzo 2014, n. 26, legislative transposition of Directive 2010/63/EU of the European Parliament and of the Council of 22 September 2010 on the protection of animals used for scientific purposes), with food and water ad libitum. The research protocol was approved by the Ethical Committee for Animal Experimentation of the University of Genoa (Prot. 319).

Preparation for CNS samples for XPCT experiment 1. Lumbar/sacrocoxygeal (L1–S4) spinal cords from naïve and EAE-induced mice at 3 dpi, 7 dpi and clinical onset ($n = 3$ for each group) were fixed in 4% paraformaldehyde for 24 h, then stored in 70% ethanol until XPCT. Just before the measurements, the samples were embedded in agarose gel, which keeps them hydrated and prevents radiation damage and movement during the experiment.

Preparation for CNS and gut samples for XPCT experiment 2 and 3. Lumbar/sacrocoxygeal (L1–S4) spinal cords, brains, and ileum samples from naïve and EAE-induced mice at 3 dpi, 7 dpi and clinical onset ($n = 2$ for each group) were dehydrated through a graded ethanol series (70/95/100%), put in propylene oxide, and included in paraffin.

Preparation for eye samples for XPCT experiment 4. Eyes with optic nerve from naïve and EAE-induced mice at the onset were embedded in paraffin and in epon. $n = 2$ samples for each group (naïve and EAE) were dehydrated through a graded ethanol series (70/95/100%), put in propylene oxide, and included in paraffin. The remaining samples, also in this case $n = 2$ for each group, were instead fixed in glutaraldehyde (2.5% in 0.1 M cacodylate buffer, pH 7.4 TA; 2 h), postfixed in osmium (1% in 0.1 M cacodylate buffer, pH 7.4; 2 h) and uranyl acetate (1% in water; overnight), dehydrated through a graded ethanol series (70/96/100%), put in propylene oxide, and embedded in resin (Propylene + EPON) at 42 °C overnight and for 48 h at 60 °C. It was found that resin embedding helps to better preserve the integrity of the eye shape.

Experimental set-ups. The XPCT experiments were performed (1) at the medical beamline ID17 of the European Synchrotron Radiation Facility (ESRF, Grenoble, France), (2) at the ANATOMIX beamline of Synchrotron SOLEIL (Paris, France), (3) at I13-2 beamline of Diamond Light Source (Didcot, UK) and (4) at SYRMEP beamline of Elettra Synchrotron (Trieste, Italy) in free-space propagation mode⁴¹.

(1) Data acquisition at ID17 was carried out using monochromatic incident X-ray beam with an energy of 35 keV. The sample-detector distance was set at 2.3 m. The detector had an effective pixel size of 3.05 µm^{42,43}. The tomography was produced by means of 2000 projections covering a total angle range of 180°. The acquisition time for each angular position was 300 ms. Data preprocessing, phase retrieval and tomographic reconstruction were performed with SYRMEP Tomo Project software and optimized scripts.

(2) The XPCT experiment at ANATOMIX beamline was performed with a filtered white beam peaked around 20 keV. The measurements were performed with an effective pixel size of 3.08 µm and 0.65 µm, resulting from 2× and 10× optics coupled with Orca Flash 4.0 camera (sensor type CMOS, sensor array size 2048 × 2048, pixel size 6.5 micron 16-bit nominal dynamic range). The propagation distance was set at 0.2 m and at 35 mm respectively. The experiment was carried out recording 4000 projections in extended field-of-view (FOV) mode, an experimental procedure of acquisition which allows to almost double the effective horizontal width of the FOV of the detector. The rotation axis is moved close to either left or right side of the FOV and a dataset of projections, having size equal to the detector FOV, is collected over 360°. After properly stitching the sinograms, the reconstruction procedure can be performed as usual. The exposure time was 100 ms per projection. Data pre-processing, phase retrieval and tomographic reconstruction were performed with PyHST software package.

(3) The experiment at I13-2 beamline used X-ray filtered-white beam peaked around 27 keV. The propagation distance was set at 0.10 m. Images were detected with a PCO.Edge 5.5 (sCMOS-technology, 2560 × 2160 pixels, 6.5 µm voxel size and a 16-bit nominal dynamic range), coupled with a scintillator screen and 1.25× optics resulting in a total magnification of 8× due to the setup configuration. The effective pixel size was 2.6 µm. Tomography was performed acquiring 4001 projections, with an exposure time of 150 ms per projection. Data pre-processing, phase retrieval and tomographic reconstruction were performed with SAVU, the tomographic data processing tool developed at Diamond Light Source Ltd.

(4) The XPCT experiment at SYRMEP, Elettra, was carried using pink beam with a mean energy of 24 keV. The sample-detector distance was set at 150 mm. Images were detected with a sCMOS camera (Hamamatsu C11440-22C-Flash4.0 v2). The effective voxel size was $0.9 \times 0.9 \times 0.9 \mu\text{m}^3$. The tomographic data were produced by means of 3600 projections covering a total angle range of 360°, in extended-FOV mode. After properly stitching the sinograms, the reconstruction procedure has been performed as usual. The exposure time was 100 ms per projection. Data preprocessing, phase retrieval and tomographic reconstruction were performed with SYRMEP Tomo Project software and optimized scripts.

In all the experiments, phase retrieval was performed by using Paganin's algorithm⁴⁴, since we acquired a single defocused image per angle in free-space propagation, and radiation wavelength and material density met the requirements. This method allows the simultaneous extraction of phase and amplitude of the wave as the ratio of the phase term over the absorption term.

In the gray scale of the tomographic images, white corresponds to higher density structures and black to lower density structures.

Tomographic reconstruction of the 3D volumes was performed from the phase-retrieved angular projections using the Filtered Back Projection algorithm, as we collected a large number of projections for acquisition.

Image analysis. Image analysis and segmentation were performed using ImageJ⁴⁵. 3D rendering images were obtained using the high-end software VGStudio Max. Before extracting qualitative and quantitative information, images were pre-processed to eliminate or mitigate artifacts due to experimental conditions or computational reconstruction. Ring artifacts were removed by an improved frequency filtering⁴⁶.

To enhance the contrast and visualize structures developing in 3D and therefore lying on different tomographic slices, we exploited the z-projection of maximum intensities, which consists in projecting on the visualization plane the voxels of a set of continuous slices. Each pixel of the output image contains the maximum value found along the axis perpendicular to that pixel.

To assess the percentage of damaged vessels, spinal cord blood vessels and clouds of extravasated materials were counted in the XPCT images through manual steps performed under expert supervision (author FP).

Since cells, particularly cell nuclei, appear as very bright objects within the tomographic volume, segmentation of cells located in intestinal villi was performed on the input XPCT images by applying an intensity threshold. Cell quantification was carried out using the 3D object counter ImageJ's plug-in⁴⁷ on the binary images.

To flatten the 3D surfaces of gut and eye, we exploited an algorithm that we recently developed⁴⁸, based on conformal mesh parameterization, and SheetMeshProjection ImageJ plug-in ref.⁴⁹, which use a coarsely spaced mesh to capture the surfaces of object.

As demonstrated, XPCT images are well suitable for quantitative analysis. With the perspective of increasing the number of samples to have biological significance, image analysis and segmentation will need an automated approach through the use of machine learning algorithms, that allow for rapid processing of large amounts of data.

Assessment of PA at different time points in different organs. We introduced the PA ratio (PA_r) as parameter to compare the extent of alterations at the different anatomical sites, since we identify imaging markers of diverse nature to describe the alterations due to EAE. PA_r is defined as

$$PA_r = \frac{PA \text{ at a certain time point}}{PA \text{ at the onset}}$$

where PA has been calculated as the percentage of damaged vessels in the CNS, and in the gut as the variation of cell density with respect to the control. PA_r can be considered a measure of the intensity – for each organ - of PA detected at a given time point compared with PA measured at onset; it is a dimensionless parameter that sets as 1 the value at disease onset.

Reporting summary. Further information on research design is available in the Nature Portfolio Reporting Summary linked to this article.

Data availability

The authors declare that the data supporting the findings of this study are available from the corresponding authors on reasonable request.

Code availability

The code developed for this work is available upon request to the corresponding authors.

Received: 5 July 2022; Accepted: 31 October 2022;

Published online: 18 November 2022

References

- Dendrou, C. A., Fugger, L. & Friese, M. A. Immunopathology of multiple sclerosis. *Nat. Rev. Immunol.* **15**, 545–558 (2015).
- Parodi, B. & Kerlero de Rosbo, N. The gut-brain axis in multiple sclerosis. Is its dysfunction a pathological trigger or a consequence of the disease? *Front. Immunol.* **12**, 1–15 (2021).
- Nouri, M., Bredberg, A., Weström, B. & Lavasani, S. Intestinal barrier dysfunction develops at the onset of experimental autoimmune encephalomyelitis, and can be induced by adoptive transfer of auto-reactive T cells. *PLoS One* **9**, e106335 (2014).
- Duc, D. et al. Disrupting myelin-specific Th17 cell gut homing confers protection in an adoptive transfer experimental autoimmune encephalomyelitis. *Cell Rep.* **29**, 378–390.e374 (2019).
- Gupta, G., Gelfand, J. M. & Lewis, J. D. Increased risk for demyelinating diseases in patients with inflammatory bowel disease. *Gastroenterology* **129**, 819–826 (2005).
- Moris, G. Inflammatory bowel disease: an increased risk factor for neurologic complications. *World J. Gastroenterol.* **20**, 1228 (2014).
- London, A., Benhar, I. & Schwartz, M. The retina as a window to the brain—from eye research to CNS disorders. *Nat. Rev. Neurol.* **9**, 44–53 (2013).
- Quinn, T. A., Dutt, M. & Shindler, K. S. Optic neuritis and retinal ganglion cell loss in a chronic murine model of multiple sclerosis. *Front. Neurol.* **2**, 50 (2011).
- Larabee, C. M. et al. Myelin-specific Th17 cells induce severe relapsing optic neuritis with irreversible loss of retinal ganglion cells in C57BL/6 mice. *Mol. Vis.* **22**, 332–341 (2016).
- Soares, R. M. G. et al. Optical neuritis induced by different concentrations of myelin oligodendrocyte glycoprotein presents different profiles of the inflammatory process. *Autoimmunity* **46**, 480–485 (2013).
- Jin, J. et al. Glial pathology and retinal neurotoxicity in the anterior visual pathway in experimental autoimmune encephalomyelitis. *Acta Neuropathol. Commun.* **7**, 1–17 (2019).
- Green, A. J., McQuaid, S., Hauser, S. L., Allen, I. V. & Lyness, R. Ocular pathology in multiple sclerosis: retinal atrophy and inflammation irrespective of disease duration. *Brain* **133**, 1591–1601 (2010).
- Di Fonzo, S. et al. Submicrometre resolution phase-contrast radiography with the beam from an X-ray waveguide. *J. Synchrotron Rad.* **5**, 376–378 (1998).
- Begani Provinciali, G. et al. X-ray phase contrast tomography for the investigation of amyotrophic lateral sclerosis. *J. Synchrotron Radiat.* **27**, 1042–1048 (2020).
- Bukreeva, I. et al. Quantitative 3D investigation of Neuronal network in mouse spinal cord model. *Sci. Rep.* **7**, 1–10 (2017).
- Fratini, M. et al. Simultaneous submicrometric 3D imaging of the microvascular network and the neuronal system in a mouse spinal cord. *Sci. Rep.* **5**, 1–7 (2015).
- Cedola, A. et al. X-ray phase contrast tomography reveals early vascular alterations and neuronal loss in a multiple sclerosis model. *Sci. Rep.* **7**, 1–11 (2017).
- Massimi, L. et al. Exploring Alzheimer's disease mouse brain through X-ray phase contrast tomography: From the cell to the organ. *Neuroimage* **184**, 490–495 (2019).
- Massimi, L. et al. Assessment of plaque morphology in Alzheimer's mouse cerebellum using three-dimensional X-ray phase-based virtual histology. *Sci. Rep.* **10**, 1–10 (2020).
- Kerlero de Rosbo, N., Bernard, C., Simmons, R. & Carnegie, P. Concomitant detection of changes in myelin basic protein and permeability of blood-spinal cord barrier in acute experimental autoimmune encephalomyelitis by electroimmunoblotting. *J. Neuroimmunol.* **9**, 349–361 (1985).
- Palermo, F. et al. X-ray phase contrast tomography serves preclinical investigation of neurodegenerative diseases. *Front. Neurosci.* **14**, 584161 (2020).
- Floris, S. et al. Blood-brain barrier permeability and monocyte infiltration in experimental allergic encephalomyelitis: a quantitative MRI study. *Brain* **127**, 616–627 (2004).
- Sibaev, A. et al. Nociceptin effect on intestinal motility depends on opioid-receptor like-1 receptors and nitric oxide synthase co-localization. *World J. Gastrointest. Pharmacol. Ther.* **6**, 73 (2015).
- Wang, H. et al. The timing and location of glial cell line-derived neurotrophic factor expression determine enteric nervous system structure and function. *J. Neurosci.* **30**, 1523–1538 (2010).
- Miyauchi, E. et al. Gut microorganisms act together to exacerbate inflammation in spinal cords. *Nature* **585**, 102–106 (2020).
- Kerlero de Rosbo, N., Jago, M. V., Carnegie, P. R. & Bernard, C. C. Correlation of the onset of experimental autoimmune encephalomyelitis-like clinical signs with oedema of the spinal cord in tunicamycin-poisoned rats. *J. Neurol. Sci.* **78**, 281–294 (1987).
- Errede, M. et al. Blood-brain barrier alterations in the cerebral cortex in experimental autoimmune encephalomyelitis. *J. Neuropathol. Exp. Neurol.* **71**, 840–854 (2012).
- Ferrara, G. et al. NG2, a common denominator for neuroinflammation, blood-brain barrier alteration, and oligodendrocyte precursor response in EAE, plays a role in dendritic cell activation. *Acta Neuropathol.* **132**, 23–42 (2016).
- Boroujerdi, A., Welser-Alves, J. V. & Milner, R. Extensive vascular remodeling in the spinal cord of pre-symptomatic experimental autoimmune encephalomyelitis mice; increased vessel expression of fibronectin and the α5β1 integrin. *Exp. Neurol.* **250**, 43–51 (2013).
- Bennett, J. et al. Blood-brain barrier disruption and enhanced vascular permeability in the multiple sclerosis model EAE. *J. Neuroimmunol.* **229**, 180–191 (2010).
- Schellenberg, A. E., Buist, R., Yong, V. W., Del Bigio, M. R. & Peeling, J. Magnetic resonance imaging of blood-spinal cord barrier disruption in mice with experimental autoimmune encephalomyelitis. *Magn. Reson. Med.* **58**, 298–305 (2007).

32. Lohmeier, J. et al. Fibrin-targeting molecular MRI in inflammatory CNS disorders. *Eur. J. Nucl. Med. Mol. Imaging* **49**, 3692–3704 (2022).
33. Guy, J. MRI in experimental inflammatory and mitochondrial optic neuropathies. *NMR Biomedicine* **21**, 968–977 (2008).
34. Kerlero De Rosbo, N. et al. The myelin-associated oligodendrocytic basic protein region MOB15–36 encompasses the immunodominant major encephalitogenic epitope (s) for SJL/J mice and predicted epitope (s) for multiple sclerosis-associated HLA-DRB1* 1501. *J. Immunol.* **173**, 1426–1435 (2004).
35. Kaushansky, N. et al. Epitope specificity of autoreactive T and B cells associated with experimental autoimmune encephalomyelitis and optic neuritis induced by oligodendrocyte-specific protein in SJL/J mice. *J. Immunol.* **177**, 76 (2006).
36. Marenga, S. et al. Functional evolution of visual involvement in experimental autoimmune encephalomyelitis. *Mult. Scler. J. Exp. Transl. Clin.* **6**, 2055217320963474 (2020).
37. Cruz-Herranz, A. et al. Monitoring retinal changes with optical coherence tomography predicts neuronal loss in experimental autoimmune encephalomyelitis. *J. Neuroinflammation* **16**, 1–17 (2019).
38. Cedola, A. et al. Orientation of mineral crystals by collagen fibers during in vivo bone engineering: an X-ray diffraction imaging study. *Spectrochim. Acta Part B. Spectrosc.* **62**, 642–647 (2007).
39. Parodi, B., Sanna, A., Cedola, A., Uccelli, A., & Kerlero de Rosbo, N. Hydroxycarboxylic acid receptor 2, a pleiotropically linked receptor for the multiple sclerosis drug, monomethyl fumarate, possible implications for the inflammatory response. *Front. Immunol.* **12**, 655212 (2021).
40. Mendel, I., Kerlero de Rosbo, N. & Ben-Nun, A. A myelin oligodendrocyte glycoprotein peptide induces typical chronic experimental autoimmune encephalomyelitis in H-2b mice: Fine specificity and T cell receptor V β expression of encephalitogenic T cells. *Eur. J. Immunol.* **25**, 1951–1959 (1995).
41. Bravin, A., Coan, P. & Suortti, P. X-ray phase-contrast imaging: from pre-clinical applications towards clinics. *Phys. Med. Biol.* **58**, R1 (2012).
42. Mittone, A. et al. Characterization of a sCMOS-based high-resolution imaging system. *J. Synchrotron Rad.* **24**, 1226–1236 (2017).
43. Mittone, A. et al. Multiscale pink-beam microCT imaging at the ESRF-ID17 biomedical beamline. *J. Synchrotron Rad.* **27**, 1347–1357 (2020).
44. Paganin, D., Mayo, S. C., Gureyev, T. E., Miller, P. R. & Wilkins, S. W. Simultaneous phase and amplitude extraction from a single defocused image of a homogeneous object. *J. Microsc.* **206**, 33–40 (2002).
45. Rueden, C. T. & Eliceiri, K. W. ImageJ for the next generation of scientific image data. *Microsc. Microanal.* **25**, 142–143 (2019).
46. Massimi, L., Brun, F., Fratini, M., Bukreeva, I. & Cedola, A. An improved ring removal procedure for in-line x-ray phase contrast tomography. *Phys. Med. Biol.* **63**, 045007 (2018).
47. Bolte, S. & Cordelières, F. P. A guided tour into subcellular colocalization analysis in light microscopy. *J. Microsc.* **224**, 213–232 (2006).
48. Stabile, S. et al. A computational platform for the virtual unfolding of Herculeum Papyri. *Sci. Rep.* **11**, 1–11 (2021).
49. Wada, H. & Hayashi, S. Net, skin and flatten, ImageJ plugin tool for extracting surface profiles from curved 3D objects. *MicroPubl. Biol.* **2020**, 1–3 (2020).

Acknowledgements

We acknowledge the European Synchrotron Radiation Facility for provision of synchrotron radiation facilities, and we would like to thank Alberto Bravin and the staff for assistance in using beamline ID 17 and constructive discussion. We acknowledge SOLEIL Synchrotron for provision of synchrotron radiation facilities, and we would like to thank

the staff for assistance in using beamline ANATOMIX (proposal 20190809). This work was carried out with the support of Diamond Light Source, beamline I13-2 (proposal MG23997-1), and we would like to thank the staff of beamline I13-2 for the support and technical assistance received during the experiment. We also want to thank G. Ferrara for induction of EAE in mice. We acknowledge for financial support: the FISIR Project “Tecnopolo di nanotecnologia e fotonica per la medicina di precisione” (funded by MIUR/CNR, CUP B83B17000010001); the TECNOMED project (funded by Regione Puglia, CUP B84I18000540002); the bilateral project CNR/RFBR (2018–2020) – accordo CNR-RFBR delle Relazioni Internazionali (CUP B86C17000210005); the project DAR-IAH IT (funded by MUR D.D. n. 2595 PON CIR01_00022) Developing national and Regional Infrastructural nodes of dAriaH in Italy (CUP B82F20000800001). ANATOMIX is an Equipment of Excellence (EQUIPEX) funded by the “Investments for the Future” program of the French National Research Agency (ANR), project “NanoimagesX”, grant no. ANR-11-EQPX-0031.

Author contributions

F.P., A.C., and N.K.deR. conceived and designed the experiments, performed the data analysis, participated to the discussion of the results and wrote the manuscript. F.P., N.P., A.S., G.B.P., L.Mas, L.Mau, E.L., L.D.A., G.S., J.P., G.T., M.F., and L.B. performed the experiments and contributed to the data analysis. B.P. and C.V. prepared the samples. G.P.M. and G.G. contributed to the data interpretation. All the authors reviewed the manuscript.

Competing interests

The authors declare no competing interests.

Additional information

Supplementary information The online version contains supplementary material available at <https://doi.org/10.1038/s42005-022-01070-3>.

Correspondence and requests for materials should be addressed to Francesca Palermo, Nicole Kerlero de Rosbo or Alessia Cedola.

Peer review information *Communications Physics* thanks Maria de la Iglesia-Vayá and the other, anonymous, reviewer(s) for their contribution to the peer review of this work.

Reprints and permission information is available at <http://www.nature.com/reprints>

Publisher's note Springer Nature remains neutral with regard to jurisdictional claims in published maps and institutional affiliations.



Open Access This article is licensed under a Creative Commons Attribution 4.0 International License, which permits use, sharing, adaptation, distribution and reproduction in any medium or format, as long as you give appropriate credit to the original author(s) and the source, provide a link to the Creative Commons license, and indicate if changes were made. The images or other third party material in this article are included in the article's Creative Commons license, unless indicated otherwise in a credit line to the material. If material is not included in the article's Creative Commons license and your intended use is not permitted by statutory regulation or exceeds the permitted use, you will need to obtain permission directly from the copyright holder. To view a copy of this license, visit <http://creativecommons.org/licenses/by/4.0/>.

© The Author(s) 2022